Optical Engineering

OpticalEngineering.SPIEDigitalLibrary.org

Expandable high-capacity wavelength division multiplex-over-optical code division multiple access millimeter wave radio-over-fiber system

Morad Khosravi Eghbal
Mehdi Shadaram

SPIE.

Morad Khosravi Eghbal, Mehdi Shadaram, "Expandable high-capacity wavelength division multiplex-over-optical code division multiple access millimeter wave radio-over-fiber system," *Opt. Eng.* **58**(1), 016118 (2019), doi: 10.1117/1.OE.58.1.016118.

Expandable high-capacity wavelength division multiplex-over-optical code division multiple access millimeter wave radio-over-fiber system

Morad Khosravi Eghbal* **and Mehdi Shadaram**
University of Texas at San Antonio, Electrical and Computer Engineering Department, One UTSA Circle, San Antonio, Texas, United States

Abstract. The design and performance evaluation of a W-band wavelength division multiplexed-over-optical code division multiple access radio-over-fiber system are presented. The system's performance introduces expansion in the number of channels and bit rate per channel for millimeter wave signals by optically encoding signals in a multiwavelength transmission system. The performance of the system is verified based on software simulation of three channels that carry six users' encoded data. The achieved results are measured in bit-error-rate and eye-diagram figures. The obtained results are analyzed for each wavelength channels and each code families used. Bit error rates of 10^{-2} to 10^{-6} are obtained for channels operating at 10 Gb/s. [DOI: 10.1117/1.OE.58.1.016118]

Keywords: millimeter wave; radio-over-fiber; optical code division multiple access; wavelength division multiplexing.

Paper 181256 received Aug. 30, 2018; accepted for publication Dec. 20, 2018; published online Jan. 31, 2019.

1 Introduction

In recent years, there has been a tremendous change in the volume of data flow in mobile communication networks.[1–7] The users in these networks require more and more bandwidth and higher data rates to stream a large amount of real-time data, with minimum latency, and seamlessly with their smartphones and other devices. Also, they need to have coverage everywhere regardless of the speed they are traveling with.[7]

The conditions of an acceptable mobile communication are no longer a smooth voice channel or fast delivery of text. Nowadays, large-sized (and thus high-quality) multimedia files are transferred more than text or voice in networks.[3–5] The live streaming and web services and apps such as Facetime or YouTube that need low latency, high bit rates, and larger bandwidth to seamlessly function are redefining mobile communication networks in terms of capacity and availability.[7]

Moreover, the ability of the system to secure transmissions from being monitored is another major constraint that must be fulfilled in the current network. The introduction of newer coding schemes or to transform the medium or signal to have an elevated level of security are part of struggles that researchers are putting toward making the mobile communication safer and more reliable.[1,4]

Currently, with the wide range of applications designed to function near a few gigahertz in the frequency spectrum, the map of this specific range in the spectrum is overly congested. Thus, designing new applications working in this frequency range is no longer feasible because of interference and power levels. However, to increase the capacity and to face less interference and licensing issues, the only natural solution is to move to a higher frequency range. In the millimeter wave ranges (from 30 up to 300 GHz) and specifically in the V-band (57 to 64 GHz) and W-band (75 to 110 GHz), the spectrum is not as busy as the lower frequency level, and additionally, there are unlicensed windows within these bands that exempt users to monitor transmission power levels. Furthermore, the higher operation frequency presents more capacity to the system to increase the bitrate or bandwidth.[8–20,21,22]

Another advantage of moving to these two bands is the inherent security of the signal in this range. The millimeter wave signal has a relatively very short propagation distance over-the-air due to the atmospheric substances. The millimeter wave signal is prone to oxygen and water in its frequency spectrum and is harshly attenuated in some specific frequencies. Therefore, its propagation distance before being recovered at the receiver is limited to about a kilometer. In addition, the millimeter wave beams projected and received by antennas are very sharp and focused; thus, the transmitting and receiving antennas should be in a line-of-sight configuration with a precise angle of arrival of the beam. This also increases the immunity of millimeter wave signals and enhances the security of the system.[14,15,23] Also, to further increase the capacity and security of the system, other schemes such as coding can be applied to the system. One efficient method is to introduce optical encoding in compliance with the optical code division multiple access (OCDMA) scheme. In this method, the optical encoding applied on the optical signal serves both for capacity expansions by accommodating more users per channel based on the number of optical codes and for the enhanced security of each user's signal as it would be only decoded with a correct corresponding optical code at the decoder.[24–31,32,23] Optical encoding/decoding is degrading the performance of the system in general when encoding the signal of each user; the bandwidth of the signal increases as it has to be expanded (spread) according to the OCDMA scheme. Thus, the bandwidth efficiency decreases when encoded signals are transmitted. In addition, encoder and decoders (SSFBGs) also introduce around 10-dB loss to the signal.

*Address all correspondence to Morad Khosravi Eghbal, E-mail: morad.khosravieghbal@utsa.edu

Finally, to increase the capacity of the system even more, the introduction of multiple wavelength channels that each can transmit many users' signals according to wavelength division multiplexing (WDM) seems inevitable. According to the ITU-T regulation, the guard band between consecutive optical channels could be made smaller to pack as many as hundreds of optical channels in the spectrum of L- and C-bands. The smaller guard bands that can still fulfill the requirements of signal detection can provide expanded capacity. However, if we combine the previous scheme (OCDMA) and WDM, we can benefit from both technologies to increase the overall network capacity. This means that we can have hundreds of channels that each accommodates transmitting the data of many users (depending on the code length, size, etc.) simultaneously.[29]

In this paper, we present a system where the data from 18 users are encoded using a seven-chip quaternary phase shift (QPS) code in a superstructure fiber Bragg grating (SSFBG). Then, they are transmitted over three wavelength channels (six users per each wavelength at C-band), multiplexed through a fiber with 20 km of length to the receiving side. At the receiving side, the optical signal is first demultiplexed to retrieve three wavelength channels, and then the encoded signals of 18 users are decoded at another seven-chip SSFBG designed according to the encoding code's profile but inverted into the original peaks (for "1"s) and noise (for "0"s).

The regenerated bit sequence for each user is then directed to a photodiode to be heterodyned with an uncoded reference carrier to generate the signal at the millimeter wave frequency of choice. The generated electrical signal at this frequency can then be retransmitted through millimeter wave antennas to the final user or it can be coherently detected and passed to a digital signal processing for further calculations.

To evaluate the signal in terms of power level, errors, and effectiveness of encoding/decoding processes, we demonstrated the bit error rate (BER) and eye diagram for one of the channels and the encoded and decoded profiles for two sets of codes in the family "A" of QPS codes. The BER levels are in the range of 10^{-6} at electrical receive power levels of about 8 μw.

The proposed system can help in increasing the capacity of the last mile networks in 5G. As it is provisioned, pico- and nano-cells are the prominent architecture for the future 5G cellular network. Thus, these cells are located very close to each other. The proposed system addresses this issue by employing E-band millimeter wave signals with very high over-the-air attenuation that guarantees small propagation area and prevents interference with neighboring cells' band. In addition, the proposed system can provide a large amount of data needed to be delivered to each cell to guarantee a seamless transmission of services that require large bandwidth and high data rates in 5G. The proposed system, offering 180 Gb/s over a 20-km fiber length, can deliver the required bandwidth for a pico/nano cell in 5G. The reconfigurability of the system comes from the fact that the system can accommodate millimeter waves with various frequency bands by just changing the sinewave generators attached to the tandem DE-MZMs. This way, by a precise calculation of the phase shifts associated with the output spectrum of the two DE-MZMs, the frequency band also changes.

In addition, the number of wavelength channels or the number of users can increase easily by just adding more wavelength channels (according to the provisions of dense wavelength division multiplexing (DWDM) and μDWDM in C and L bands) or encoders/decoders to each channel. Thus, the system has the ability to be reconfigured (expanded in the number of users/channels), provided that the measurements at the receiver are still acceptable for detection and generation of millimeter waves.

2 Theoretical Analysis

The SSFBG that performs the encoding and decoding is a small device made of a short length (in millimeter range) of optical fiber that has repetitive varying refractive indices throughout its length. The change in the refractive index at each chip is made by shining ultraviolet light for a specific duration of time and with a particular beam power to etch the change in the refractive index at the target chip. The major difference between a fiber Bragg grating and a superstructure fiber Bragg grating is that each chip (section with a constant refractive index) of the SSFBG has a sinusoidal varying refractive index with a very small period (in nanometer range) relative to the default refractive index. An SSFBG is illustrated in Fig. 1. The optical signal, in the form of the short pulses incident to the beginning of the SSFBG, enters a medium with a different refractive index compared with the air; thus, it experiences reflection, refraction, and transmittance all together. The portion of the power that is transmitted through the first chip reaches to the interface of the first and second chip, where due to the difference in the refractive indices of two media, it experiences the same phenomena all over again. This continues to happen to the remaining power of the initial optical pulse that survives to be transmitted until the last chip. The phase shift that the optical pulse experiences at the border of the two consecutive chips depends on the QPS code that is applied to this encoder. The phase shifts can be one of the four values (0, $\frac{\pi}{2}$, π, and $\frac{3\pi}{2}$).

The reflection profile of the light off the SSFBG is identical to the generating seven-segment code that the SSFBG is configured with. Thus, each individual code creates a specifically identical profile that can only be decoded, with the same code but inversely applied to the SSFBG to regenerate the initial optical pulse.

To mathematically analyze SSFBG, we need to start with the coupled mode theory. By following the notation of Erdogan[33] and Kogelnik[34] and assuming that we can write the transverse component of the electric field as a superposition of the ideal modes, where there is no perturbation in the grating, and label them with γ, we will have

$$\vec{\mathbf{E}}_t(x,y,z,t) = \sum_{\gamma}[A_\gamma(z)\exp(j\beta_\gamma z) + B_\gamma(z)\exp(-j\beta_\gamma z)].\mathbf{e}\gamma t(x,y)\exp(-j\omega t), \tag{1}$$

where $A\gamma(z)$ and $B\gamma(z)$ are the slowly varying amplitudes of the γ'th mode traveling in the $\pm z$ direction. Now, if we assume that the modes are not ideal and thus there are dielectric perturbations, Eq. (1) will be

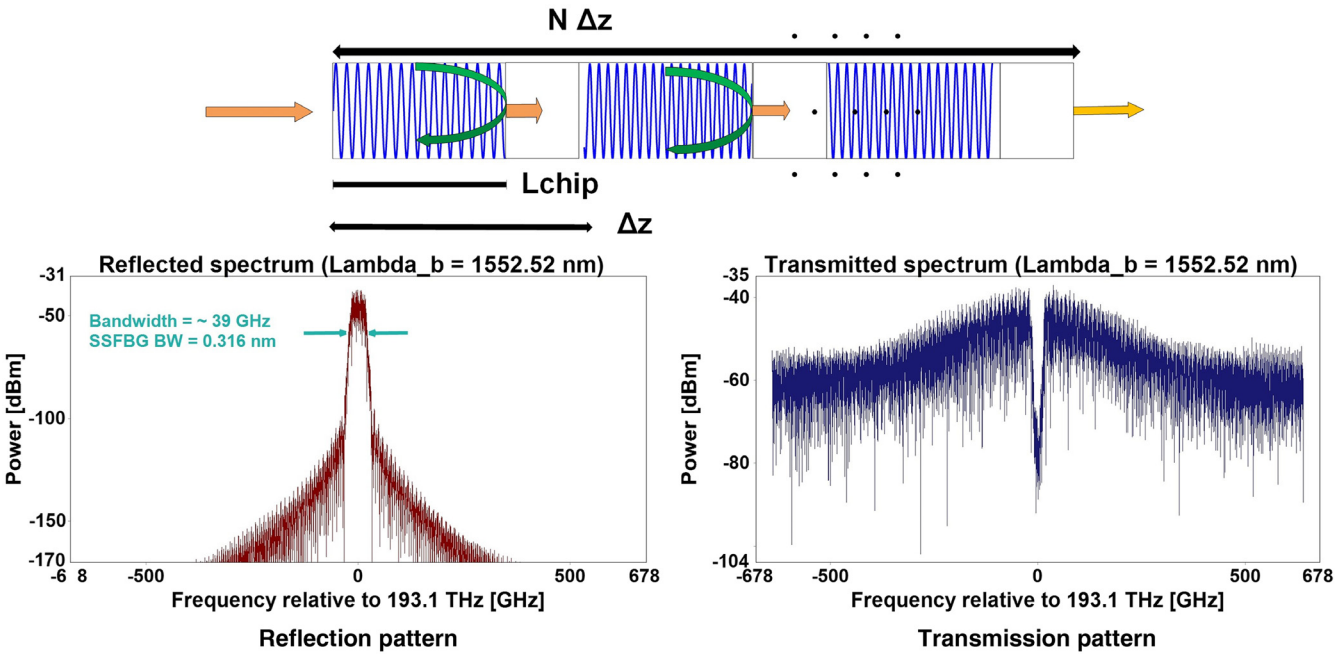

Fig. 1 SSFBG schematic diagram. Reflected and transmitted beams as well as reflection and transmission pattern are shown.

$$\frac{dA_\gamma}{dz} = j\sum_\zeta A_\zeta (K^t_{\zeta\gamma} + K^z_{\zeta\gamma}) \exp[j(\beta_\zeta - \beta_\gamma)z] + j\sum_\zeta B_\zeta (K^t_{\zeta\gamma} - K^z_{\zeta\gamma}) \exp[-j(\beta_\zeta + \beta_\gamma)z], \tag{2}$$

$$\frac{dB_\gamma}{dz} = -j\sum_\zeta A_\zeta (K^t_{\zeta\gamma} - K^z_{\zeta\gamma}) \exp[j(\beta_\zeta + \beta_\gamma)z] - j\sum_\zeta B_\zeta (K^t_{\zeta\gamma} + K^z_{\zeta\gamma}) \exp[-j(\beta_\zeta - \beta_\gamma)z], \tag{3}$$

where $K^t_{\zeta\gamma}(z)$ is the transverse coupling coefficient and $K^z_{\zeta\gamma}(z)$ is the longitudinal coupling coefficient between two modes of ζ and γ.

Now, in a Bragg grating, the components that are dependent to z, which is oscillating very fast will be neglected because they are not contributing to the changes in the amplitudes $A(z)$ and $B(z)$ around the wavelength where the dominant interaction is the counter-interaction between mode of amplitudes. So, Eqs. (2) and (3) will become

$$\frac{dR}{dz} = j\hat{\sigma}R(z) + j\kappa S(z), \tag{4}$$

$$\frac{dS}{dz} = -j\hat{\sigma}S(z) - j\kappa^* R(z), \tag{5}$$

where $R(z) = A(z)\exp(j\delta z - \varphi/2)$ and $S(z) = B(z) \times \exp(-j\delta z + \varphi/2)$. Also, κ represents coupling coefficient that is changing with time ("AC") and σ represents the coefficient that self-couples the component ("DC"):

$$\hat{\sigma} = \delta + \sigma - \frac{1}{2}\frac{d\varphi}{dz}, \tag{6}$$

$$\delta = \beta - \frac{\pi}{\lambda} = \beta - \beta_D = 2\pi n_{\text{eff}}\left(\frac{1}{\lambda} - \frac{1}{\lambda_D}\right), \tag{7}$$

$$\kappa = \kappa^* = \frac{\pi}{\lambda} v\overline{\delta n}_{\text{eff}}. \tag{8}$$

If the grating is uniform along the length, then $\overline{\delta n}_{\text{eff}}$ is constant and $\frac{d\varphi}{dz} = 0$ so κ, σ, and $\hat{\sigma}$ will be constants. Therefore, from Eqs. (2) and (3), the reflectivity off a uniform Bragg grating with length L and assuming that the boundary conditions are $R(-L/2) = 1$ and $S(L/2) = 0$ only will be for a forward-propagating wave and not for a backward-propagating wave for $z \geq L/2$. Thus, we can write the amplitude and power reflection coefficients $\rho = S(-L/2)/R(-L/2)$ and $r = |\rho|^2$ we have

$$\rho = \frac{-\kappa \sinh\left(L\sqrt{\kappa^2 - \hat{\sigma}^2}\right)}{\hat{\sigma}\sinh\left(L\sqrt{\kappa^2 - \hat{\sigma}^2}\right) + j\sqrt{\kappa^2 - \hat{\sigma}^2}\cosh\left(L\sqrt{\kappa^2 - \hat{\sigma}^2}\right)}, \tag{9}$$

$$r = \frac{\sinh^2\left(L\sqrt{\kappa^2 - \hat{\sigma}^2}\right)}{\cosh^2\left(L\sqrt{\kappa^2 - \hat{\sigma}^2}\right) - \frac{\hat{\sigma}^2}{\kappa^2}}. \tag{10}$$

With Eqs. (9) and (10), we can define the power reflection model of an SSFBG device that has many chips distributed over the entire length of the device. However, if we assume that one of the chips has the length L_{chip}, we can define $\hat{\sigma}$ with $\lambda_{\max}$ (wavelength at the maximum reflectivity) and NG (total number of grating periods) as follows:[35]

$$\hat{\sigma} = \left(\frac{\lambda_{\max}}{\lambda} - 1\right)\pi\frac{N_G}{L_{\text{chip}}}, \tag{11}$$

$$\lambda_{\max} = \left(1 + \frac{\overline{\delta n_{\text{eff}}}}{n_{\text{eff}}}\right)\lambda_D, \tag{12}$$

where λ_D is the design wavelength and is almost equal to $\lambda_{\max}$. Figure 1 shows the schematic of a piece of SSFBG where the distance between two consecutive chips is Δz_0 and there are M chips with the length of L_{chip}. The sinusoidal varying refractive index along a chip relative to the effective refractive index is Δn that is much smaller than the effective refractive index $\overline{n}_{\text{eff}}$. The light that etches each chip has a wavelength equal to $\lambda_i = \lambda_D + i\Delta\lambda$, where $\lambda_D \ll \Delta\lambda$. Also, the phase shift φ between two consecutive chips is shown.

From Eqs. (9) and (10) and applying the Taylor series to sinh() and cosh() when the nominator is small, we will have the following:

$$r_{\text{chip}}(\lambda) = \left|\frac{-\kappa_1 L_{\text{chip}}}{\pi\left\{\left(\frac{N_G}{L_{\text{chip}}}\right)\left[\left(\frac{\lambda_{\max}}{\lambda}\right) - 1\right]\right\} + j}\right|^2. \tag{13}$$

which resembles the transfer function of a bandpass filter (BPF) that has the center wavelength of $\lambda_{\max}$ that becomes $r_{\text{chip}}(\lambda_{\max}) = |\kappa_1 L_{\text{chip}}|^2$, and at the $\pm\infty$, the reflection function becomes

$$r_{\text{chip}}(\pm\infty) = \frac{|\kappa_1 L_{\text{chip}}|^2}{\left(\pi\frac{N_G}{L_{\text{chip}}}\right)^2 + 1} = \varepsilon|\kappa_1 L_{\text{chip}}|^2, \tag{14}$$

where $\varepsilon = \frac{1}{(\pi\frac{N_G}{L_{\text{chip}}})^2+1} \ll 1$ so we can use BPF transfer function for an SSFBG device. We also consider that all the chips have been etched with the same wavelength λ_i and all have the same $\kappa = \kappa_1$.

We can similarly write the transfer function of the first chip according to the analogy with a BPF assuming the first phase shift would be $\varphi_1 = 0$. It becomes a weighted rectangular function as follows:[35]

$$\text{Rect}_\varepsilon\left(\frac{\lambda - \lambda_{\max}}{B}\right) = \begin{cases} 1 \text{ when } \lambda_{\max} - \frac{B}{2} \le \lambda \le \lambda_{\max} + \frac{B}{2} \\ \varepsilon \text{ other } \lambda \end{cases}, \tag{15}$$

where ε is the minimum amplitude and B is the bandwidth equal to

$$B \cong \left(\frac{2L_{\text{chip}}}{\pi N_G}\right)\lambda_{\max}. \tag{16}$$

And thus the 3-dB bandwidth happens at $\lambda = \lambda_{\max} \pm (B/2)$. Each section of the SSFBG performs like a filter having the following transfer function:

$$|\kappa_1 L_{\text{chip}}|^2 \times \exp\{j\varphi_i\} \times \text{Rect}_\varepsilon\left(\frac{\lambda - \lambda_D - i\Delta\lambda}{B}\right). \tag{17}$$

Now if we assume that we have N chips in the SSFBG device, the collective power reflection function of the N series of chips becomes

$$\prod_{i=1}^{N} |\kappa_1 L_{\text{chip}}|^2 \times \exp\{j\varphi_i\} \times \text{Rect}_\varepsilon\left(\frac{\lambda - \lambda_D - i\Delta\lambda}{B}\right). \tag{18}$$

With a special case where $(B/2) < \Delta\lambda < B$, the collective power reflection function can be written as

$$\sum_{i=0}^{N-1} A^2 \times \exp\{j(\varphi_i + \varphi_{i+1})\} \times \text{Rect}_{\varepsilon_2}\left[\frac{\lambda - \lambda_D - i\Delta\lambda - \left(\frac{\Delta\lambda}{2}\right)}{W}\right], \tag{19}$$

with $A^2 = \varepsilon^{N-2}\ |\kappa_1 L_{\text{chip}}|$ and $\varepsilon_2 = \varepsilon/|\kappa_1 L_{\text{chip}}|^2$ and finally $W = B - \Delta\lambda$ with $0 < W < B$ with the center wavelength at the summation of λ_D, $i\Delta\lambda$, and $(\Delta\lambda/2)$.

If we disregard ε_2, since the sampling happens at the center of rectangular pulses, then the sampling is equivalent to considering W being very small. This will change Eq. (19) to a train of unit pulses. Therefore, the SSFBG's reflected power after N-number of segments after the sampling will be equal to

$$\sum_{i=0}^{N-1} A^2 \times \exp\{j(\varphi_i + \varphi_{I+1}\} \times \delta\left(\lambda - \lambda_D - i\Delta\lambda - \frac{\Delta\lambda}{2}\right). \tag{20}$$

If we consider $\varphi_N = \varphi_0$, that the power reflection is periodic and will be one cycle from first chip to the last, we need to assume that the codes embedded in the SSFBG are long ($N \gg 2$), and thus the inverse discrete Fourier transform (IDFT) of the normalized reflected power around $\lambda_D + (\Delta\lambda/2)$ can be regarded approximately as

$$x_{\text{SSFBG}}(n) \propto \sqrt{N} \times \text{IDFT}\left\{\sum_{i=0}^{N-1} \exp\{j(\varphi_i + \varphi_{i+1}\} \times \delta(\lambda - i\Delta\lambda)\right\}. \tag{21}$$

If the SSFBG's input is equal to a pulse with amplitude $(\sqrt{N}/A2)$, Equation (21) is a baseband signal. Also, each segment of an SSFBG when $\Delta\lambda$ ranges between $B/2$ and B has a phase of $\theta_i = \varphi_i + \varphi_{i+1}$ and constant amplitude for all segments. This indicates that the SSFBG baseband signal's reflected power is the IDFT of a unimodular sequence.

We would like to study power reflection off an SSFBG device to understand how much power is reflected off the device with specific design parameters (such as the number of periods, the length of each chip, the total number of chips, etc.) and, therefore, how much power is transmitted through the SSFBG device.

The reflected power off a train of N FBGs is given by Pereira and de Silva[35]

$$\prod_{i=1}^{N} |\kappa L_{\text{chip}}|^2 \times \exp\{j\varphi_i\} \times \text{Rect}_\varepsilon\left(\frac{\lambda - \lambda_D - i\Delta\lambda}{B}\right), \tag{22}$$

where L_{chip} is the length of one chip, φ_i is the phase of chip i, and Rect_ε is a weighted rectangular function, B is the bandwidth of the SSFBG device, λ_D is the design wavelength and finally $\Delta\lambda$ is the wavelength increment ($\Delta\lambda \ll \lambda D$). Each segment represents an SSFBG chip etched with phase φ_i.

For this work, with $\nu\delta_{\overline{n_{\text{eff}}}} = 5 \times 10^{-4}$ and $\lambda = 1551$ nm, κ can be calculated from the below equation:

$$\kappa = \kappa^* = \frac{\pi}{\lambda}\nu\overline{\delta n_{\text{eff}}}. \tag{23}$$

Therefore, by having $L_{\text{chip}} = 0.66$ mm, we can calculate $|\kappa L_{\text{chip}}|^2 = 0.446$. Also, $N = 7$, so there are only seven chips in each SSFBG device. Finally, the phase shifts φi are only four values (0, $\frac{\pi}{2}$, π, and $\frac{3\pi}{2}$).[36] The reflection and transmission pattern of a QPS code off an SSFBG is illustrated in Fig. 1.

In addition, the family of the codes used in this paper is family A of QPS codes that are first introduced by Boztas et al.[37] As shown in Table 1, there are two polynomial defining equations of these codes with three shift registers generating seven-chip long codes. Each generating characteristic polynomial-defining equation can produce nine different codes depending on the initial value sequences of the shift registers. Again, the initial values are a combination of four values (0, 1, 2, and 3). Thus, there are 18 different codes per both characteristic polynomials that are listed in Table 1.

The generating characteristic polynomial that is a primitive irreducible polynomial of degree m in $Z_4[x]$ has an equation like the following:[38]

$$h(x) = h_0 x^m + h_1 x^{m-1} + \ldots + h_{m-1}x + h_m \quad \text{and}$$
$$h_i \in Z_4, \quad h_0 = 1. \tag{24}$$

Considering the first line of Table 1, there is a characteristic polynomial of degree 3 ($m = 3$) with weights (h_i's) of 1213 as follows:

$$h(x) = x^3 + 2x^2 + x + 3. \tag{25}$$

We can consider the third-order linear occurrence over $Z_4[x]$ having characteristic polynomial of $h(x)$:

$$\begin{aligned} a_n &= -2a_{(n-1)} - a_{n-2} - 3a_{n-3} \\ &= +2a_{n-1} + 3a_{n-2} + a_{n-3} \,(\text{mod}\, 4), \qquad n \gg 3. \end{aligned} \tag{26}$$

Also, for the characteristic polynomial with 1323 (Table 1), we have

$$h(x) = x^3 + 3x^3 + 2x^2 + 3, \tag{27}$$

which has the characteristic polynomial of

$$\begin{aligned} a_n &= -3a_{n-1} - 2a_{n-2} - 3a_{n-3} \\ &= +a_{n-1} + 2a_{n-2} + a_{n-3} \,(\text{mod}\, 4), \quad n \gg 3. \end{aligned} \tag{28}$$

This linear occurrence will generate a set of sequences of period $N = 2^3 - 1$ and size $M = 2^3 + 1$ over Z_4. Different sequences in the set may be generated by loading the shift register with any set of initial condition, not identically zero and cycling the shift register through a full period N.[38] Thus, the three-tuple initial values loading the shift registers are combinations of 0, 1, 2, and 3.

Table 1 Two polynomial defining equation and all 18 generated QPS codes.[37,38]

$h(x) = x^3 + 2x^2 + x + 3$		
Code #	Gen. sequence	QPS code
1	2002022	π-0-0-π-0-π-π
2	3221211	$3\pi/2$-π-π-$\pi/2$-π-$\pi/2$-$\pi/2$
3	1223233	$\pi/2$-π-π-$3\pi/2$-π-$3\pi/2$-$3\pi/2$
4	1013102	$\pi/2$-0-$\pi/2$-$3\pi/2$-$\pi/2$-0-π
5	1100123	$\pi/2$-$\pi/2$-0-0-$\pi/2$-π-$3\pi/2$
6	2010333	π-0-$\pi/2$-0-$3\pi/2$-$3\pi/2$-$3\pi/2$
7	1112030	$\pi/2$-$\pi/2$-$\pi/2$-π-0-$3\pi/2$-0
8	2133003	π-$\pi/2$-$3\pi/2$-$3\pi/2$-0-0-$3\pi/2$
9	2303130	π-$3\pi/2$-0-$3\pi/2$-$\pi/2$-$3\pi/2$-0
$h(x) = x^3 + 3x^3 + 2x^2 + 3$		
10	2002220	π-0-0-π-π-π-0
11	1110302	$\pi/2$-$\pi/2$-$\pi/2$-0-$3\pi/2$-0-π
12	3112122	$3\pi/2$-$\pi/2$-$\pi/2$-π-$\pi/2$-π-π
13	0011321	0-0-$\pi/2$-$\pi/2$-$3\pi/2$-π-$\pi/2$
14	2322133	π-$3\pi/2$-π-π-$\pi/2$-$3\pi/2$-$3\pi/2$
15	1012013	$\pi/2$-0-$\pi/2$-π-0-$\pi/2$-$3\pi/2$
16	0331230	0-$3\pi/2$-$3\pi/2$-$\pi/2$-π-$3\pi/2$-0
17	3301023	$3\pi/2$-$3\pi/2$-0-$\pi/2$-0-π-$3\pi/2$
18	3203130	$3\pi/2$-π-0-$3\pi/2$-$\pi/2$-$3\pi/2$-0

3 Principle of Operation

Three continuous wave lasers generate the optical beams, having the center wavelengths of 1553.33, 1552.52, and 1551.72 nm, respectively. The schematic setup is shown in Fig. 2. Each laser has an output optical power equal to 8 mw with linewidths of about 7 MHz. A tandem dual-electrode Mach-Zehnder modulator (DE-MZM) is used to modulate the baseband laser beam to the radio frequency (RF) bands.

For the three wavelength channels 1, 2, and 3, each carrying six encoded users' data, the first DE-MZM is driven by two sinewave generators connected to each arm of the modulator that is biased to operate at the null point. By passing through the first DE-MZM, the baseband signals at the center wavelengths of each laser are shifted to the upper and lower sidebands.

These tones spread across the upper and lower sidebands are then fed into the second DE-MZM that is driven by another sinewave generator and its π-phase shifter version of it that feeds the other arm. After passing through the second DE-MZM, the components in the first DE-MZM's generated tones are shifted in the spectrum. The details of how much

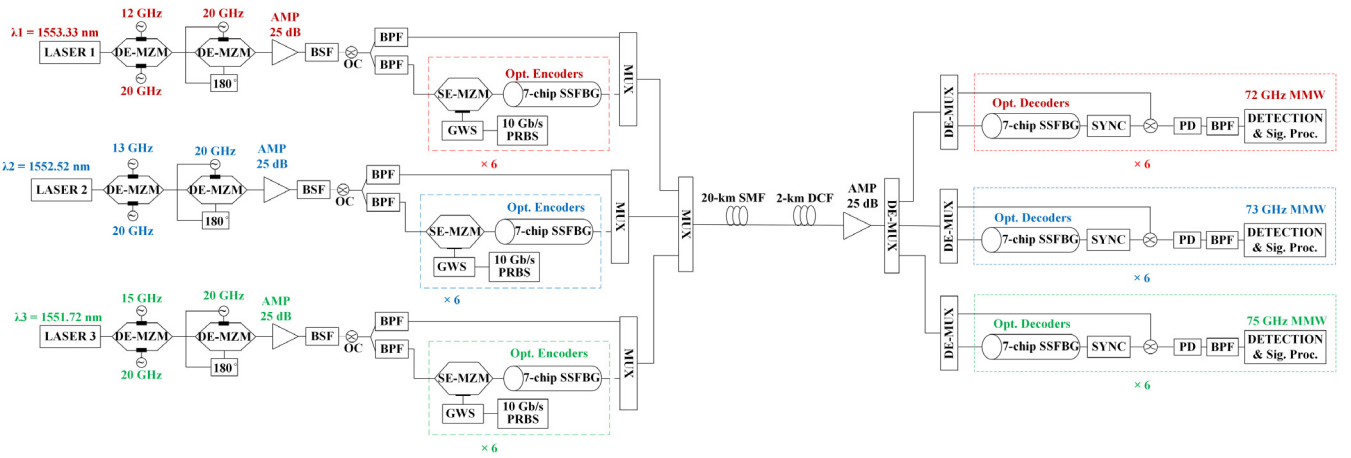

Fig. 2 Simulation setup.

each tone is shifted after the first and second DE-MZM and the final kept components for each channel are depicted in Table 2.

Figure 3 shows all the upper and lower band components for all three channels with their wavelengths marked right before the multiplexers in Fig. 2. The color codes relate to each individual channel. Thus, according to Fig. 2, red components are channel one, blue is channel two, and finally green is channel three. For each channel, both the data modulated and unmodulated components are marked.

By choosing those components for each wavelength channel, we introduced a frequency difference between them that will be translated into an electrical signal upconverted to the difference in frequency (in this case, 72, 73, and 75 GHz). Thus, the output electrical signal will be operating at the E-band window.

The wavelength components located at the lower side bands are chosen to be data modulated and optically encoded for six users. The data modulation is performed through a single electrode Mach–Zehnder modulator (SE-MZM)

Table 2 Tones shifted after the first and second DE-MZMs. The upper and lower tones that are kept for millimeter wave generation and their distance.

Wavelength channels (nm)	Tones after the first DE-MZM (GHz)	Tones after the second DE-MZM (GHz)	Tones in the frequency domain (GHz) after filter	Tones in wavelength (nm) and their distance
Ch. 1 @ 1553.33	±12, ±20, ±32, ±8	±12, ±20, ±32, ±8, ±40, ±28, ±52	−32 and +40	1553.58 and 1553.00
			72-GHz distance	0.58 nm
Ch. 2 @ 1552.52	±13, ±20, ±33, ±7	±13, ±20, ±33, ±7, ±40, ±27, ±53	−33 and +40	1552.79 and 1552.20
			73-GHz distance	0.59 nm
Ch. 3 @ 1551.72	±15, ±20, ±35, ±5	±15, ±20, ±35, ±5, ±40, ±25, ±55	−35 and +40	1552.00 and 1551.40
			75-GHz distance	0.6 nm

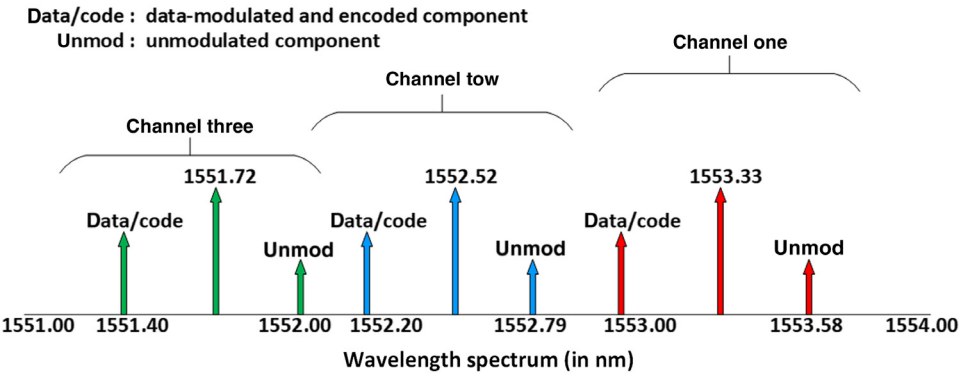

Fig. 3 Modulated and unmodulated components for each channel (in nm).

that is driven by a pseudo random bit sequence generator at 10 Gb/s and $10^{-23} - 1$ bits that are shaped by a Gaussian signal source having full-width at half maximum (FWHM) of 5.2 ps.

The data modulated signals are then passed to six (per each channel) SSFBG devices for six users that are etched with the codes in Table 1. The encoded signal has a profile relevant to the generating QPS codes that are identical. They can only be decoded with a code that can match with the profile and is inversed and etched to another SSFBG device. The encoded signals of each bundle of six users along with the component at the upper side band that is unmodulated and not coded are multiplexed at an 8×1 multiplexer. Then, the three multiplexed bundles are again multiplexed into a 4×1 multiplexer to be transmitted through a dispersion-compensated fiber with the length of 20 km that has pre-amplification of about 25 dB.

Finally, at the receiving side, the received multiplexed optical signal is demultiplexed into three six-user bundles and one unmodulated carrier, and each bundle is selected by the optical filtering per the center wavelength of the channel. Thus, 18 users' signals are passed through 18 SSFBG devices that are etched with the inversed format of the codes listed in Table 1. The outputs of the SSFBGs are decoded signals that are data modulated. Finally, these optical signals are heterodyned with the corresponding unmodulated carrier at a photodiode to generate the electrical signal, upconverted to the frequency difference between the unmodulated carrier and data-modulated components. The output of the photodiodes is RF electrical signals at 72, 73, and 75 GHz, respectively, for each channel. A bandpass filter is then used to filter the electrical millimeter wave signals. At this stage, the performance verification measures such as BER and eye diagrams of each signal are evaluated to confirm the operability of the overall system.

4 Simulation Results

VPITransmissionMaker software version 9.8 from VPI Photonics is used to design and simulate the proposed setup of this work. The setup is depicted in Fig. 2. The BER versus received electrical power (in μw) per each wavelength channel is depicted in Fig. 4. Also, the eye-diagram for various received power level is also shown on the BER curve. Finally, Fig. 5 shows a comparative figure for all channels' BER curve versus the received electrical power.

5 Discussion

Figure 4 illustrates the BER curve per received electrical power (in μm) for channel 1. It carries six users' data, encoded with QPS codes, and at the receiving side, the signals are decoded and detected at the photodiode. Then, the BER curve for various received electrical power is measured, and the eye diagram of the electrical signal is depicted.

The obtained simulation results show that the opening section of the eye diagram is gradually shrunk by the increase in the BER for the lower received electrical power (in μw) after the photodiode. This trend holds for all three channels. The BER levels that have been measured in this study are as low as 10^{-7} (for ch. 3) and 10^{-5} (for ch. 2 and ch. 1). Therefore, the indicator for the correspondence between the eye diagram at a certain BER follows the same trend in descending BER levels with increased noise both on the signal profile and on the noise floor, causing an almost eye closure at BER close to 10^{-2}. The BER versus the received electrical power is linearly changing for all three channels, and each BER curve only differs slightly with the other two. Thus, the BER at 10^{-4}, which is almost in the middle of the measured points (from 10^{-2} to 10^{-6}), is used as a reference point to find the marginal deviation between the curves of all three channels. Based on the received power, ch. 3 has the best performance. The difference in the marginal values for the higher and lower channels (ch. 1 and ch. 3, respectively) at the reference BER of 10^{-4} is about 2.1 dB. Individually, at BER of 10^{-4}, the gain margin between ch. 1 and ch. 2 is about 1.2 dB and between ch. 2 and ch. 3 is about 0.9 dB.[23]

Therefore, the multiplexing effects on the BER margin for the three wavelength channels are depicted. This gain difference is primarily because of the wavelength selective nature of the standard single-mode fiber optic cable used in this setup. This feature imposes higher attenuation to smaller wavelength channels. This can reveal that, irrespective of

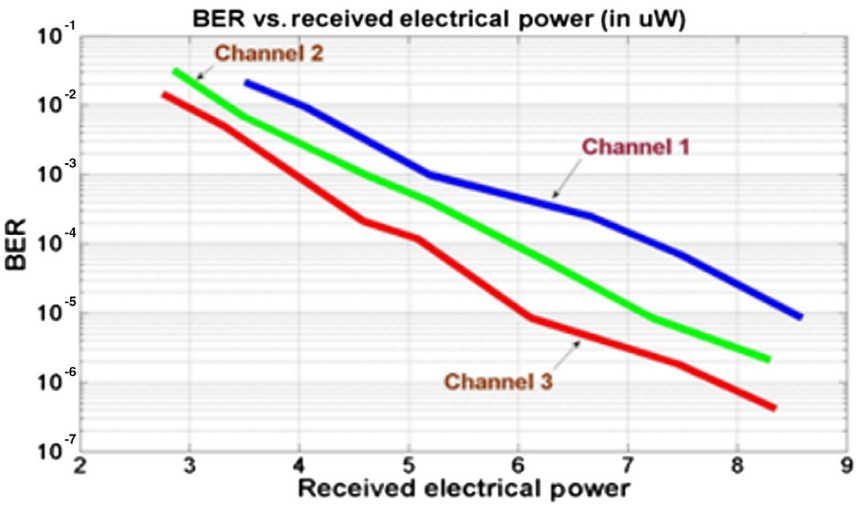

Fig. 4 BER curved for the received electrical power per all three channels.

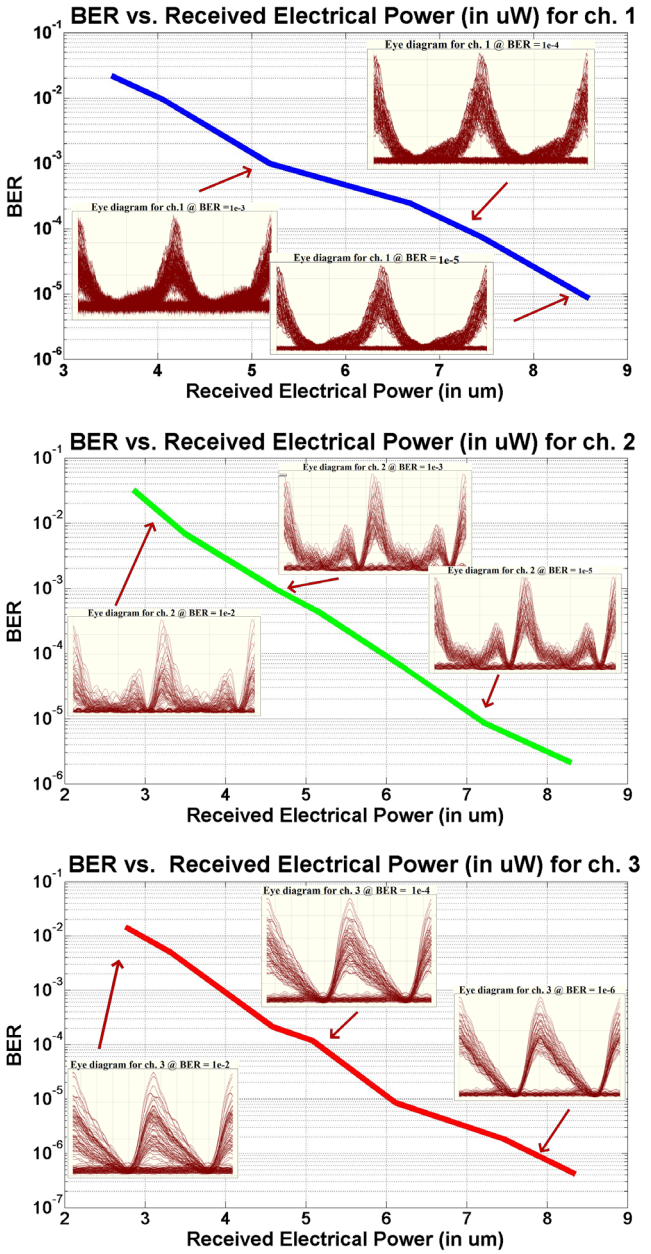

Fig. 5 BER curve for the received electrical power (in μW) per all three channels. The eye-diagram for three different received power levels are also shown for each wavelength channels.

the nature of the code, channel 3 experiences more attenuation. However, the BER curve for channel 3 is more promising for both setups (Figs. 4 and 5) since it has smaller received power per the decrease in the BER value.[23]

6 Conclusion

A W-band radio-over-fiber system is proposed that can transmit the encoded data of 18 users on three wavelength channels. Thus, each wavelength channel (in the C-band) carries six users' encoded data to the receiver. The millimeter wave upconversion happens at a tandem DE-MZMs, where two tones are selected per each channel to generate the millimeter wave electrical signal at the receiver according to their frequency difference in the spectrum. One of the tones is kept unmodulated and uncoded while the other tone (per wavelength) goes through data-modulation and encoding/decoding processes. At the receiver, these two tones are heterodyned at the photodiode to generate the millimeter wave, which is upconverted to the W-band. Since this system can be expanded both by the number of the wavelength simultaneously transmitting data (DWDM) and also by the number of encoded/decoded users (OCDMA) in addition to the millimeter wave frequency, it can offer an enormous increase in the amount of data transmission through optical fiber. Moreover, if the only major nonlinearity sources are the conventional optical fiber network components (such as optical fibers, amplifiers, photodetectors, etc.), the compensation methods are well-established and explained in the literature. Therefore, this system seems to be promising in delivering the large amount of capacity that is necessary toward the network requirements of the next generation of mobile networks (5G).

The obtained BER curves and the eye-diagram openings are used to verify the performance of the system for various received electrical power at the receiver. The BER margin between the highest and lowest wavelength channels is about 2 dB, and the lowest wavelength channel offers the best BER for the received electrical power.

References

1. T. S. Rappaport et al., "Overview of millimeter wave communications for fifth-generation (5G) wireless networks—with a focus on propagation models," *IEEE Trans. Antennas Propag.* **65**(12), 6213–6230 (2017).
2. T. S. Rappaport et al., "Small-scale, local area, and transitional millimeter wave propagation for 5G communications," *IEEE Trans. Antennas Propag.* **65**(12), 6474–6490 (2017).
3. S. Hur et al., "Proposal on millimeter-wave channel modeling for 5G cellular system," *IEEE J. Selected Top. Signal Process.* **10**(3), 454–469 (2016).
4. T. S. Rappaport et al., "Millimeter wave mobile communications for 5G cellular: it will work!," *IEEE Access* **1**, 335–349 (2013).
5. T. S. Rappaport et al., "Wideband millimeter-wave propagation measurements and channel models for future wireless communication system design," *IEEE Trans. Commun.* **63**(9), 3029–3056 (2015).
6. S. Rangan, T. S. Rappaport, and E. Erkip, "Millimeter-wave cellular wireless networks: potentials and challenges," *Proc. IEEE* **102**(3), 366–385 (2014).
7. "5G Radio access: capabilities and technologies' [white page]," Ericsson white paper Uen 284 23-3204 Rev C, https://www.ericsson.com/res/docs/whitepapers/wp-5g.pdf (17 November 2016).
8. A. Lebedev et al., "Demonstration and comparison study for V- and W-band real-time high-definition video delivery in diverse fibre-wireless infrastructure," *Fibre Integrated Opt.* **32**(2), 93–104 (2013).
9. Y. Xu et al., "Demonstration of 60 Gb/s W-band optical mm-wave signal full-duplex transmission over fibre-wireless-fibre network," *IEEE Commun. Lett.* **18**(12), 2105–2108 (2014).
10. H. T. Huang et al., "High spectral efficient W-band OFDM-RoF system with direct-detection by two cascaded single-drive MZMs," *Opt. Express* **21**(14), 16615–16620 (2013).
11. J. Yu et al., "Cost-effective optical millimeter technologies and field demonstrations for very high throughput wireless-over-fibre access systems," *J. Lightwave Technol.* **28**(16), 2376–2397 (2010).
12. Z. Jia et al., "Key enabling technologies for optical–wireless networks: optical millimeter-wave generation, wavelength reuse, and architecture," *J. Lightwave Technol.* **25**(11), 3452–3471 (2007).
13. X. Pang et al., "Multigigabit W-band (75–110 GHz) bidirectional hybrid fibre-wireless systems in access networks," *J. Lightwave Technol.* **32**(23), 4585–4592 (2014).
14. X. Li et al., "Photonics millimeter-wave generation in the E-band and bidirectional transmission," *IEEE Photonics J.* **5**(1), 7900107 (2013).
15. Y. Niu et al., "A survey of millimeter wave communications (mmWave) for 5G: opportunities and challenges," *Wireless Networks* **21**(8), 2657–2676 (2015).
16. L. Wei et al., "Key elements to enable millimeter wave communications for 5G wireless systems," *IEEE Wireless Commun.* **21**(6), 136–143 (2014).
17. Z. Pi and F. Khan, "An introduction to millimeter-wave mobile broadband systems," *IEEE Commun. Mag.* **49**(6), 101–107 (2011).

18. M. Bakaul, A. H. M. R. Islam, and A. Nirmalathas, "Recent progresses in Gigabit wireless access using millimeter-wave RoFs," in *IEEE 6th Int. Conf. Photonics (ICP)*, Kuching, pp. 1–3 (2016).
19. T. Yang, M. Gao, and J. Qian, "A simple scheme to generate two millimeter-wave signals for radio-over-fiber systems," in *8th IEEE Int. Conf. Communication Software and Networks (ICCSN)*, Beijing, pp. 478–482 (2016).
20. A. Bekkali and K. Nishimura, "Seamless convergence of radio-over-fiber and millimeter-wave links for highly resilient access networks," in *IEEE Wireless Communications and Networking Conference*, Doha, pp. 1–6 (2016).
21. T. Dat et al., "5G transport networks: the need for new technologies and standards," *IEEE Commun. Mag.* **54**(9), 18–26 (2016)
22. P. Wang et al., "Multi-gigabit millimeter wave wireless communications for 5G: from fixed access to cellular networks," *IEEE Commun. Mag.* **53**(1), 168–178 (2015).
23. M. K. Eghbal, F. Aminian, and M. Shadaram, "A method to increase the capacity of a millimeter wave radio-over-fiber system," in *20th Int. Conf. Transparent Optical Networks (ICTON)*, Bucharest, pp. 1–4 (2018).
24. C. Chen, C. Zhang, and K. Qiu, "OCDMA-based 60-GHz radio-over-fibre system for next generation wireless access networks," in *Int. Conf. Microwave and Millimeter Wave Technology (ICMMT)*, Shenzhen, China, pp. 1–4 (2012).
25. P. C. Teh et al., "A comparative study of the performance of seven- and 63-chip optical code-division multiple-access encoders and decoders based on superstructured fibre Bragg gratings," *J. Lightwave Technol.* **19**(9), 1352–1365 (2001).
26. M. K. Eghbal and M. Shadaram, "Tandem-modulator generated W-band OCDMA radio-over-fibre system," in *18th Int. Conf. Transparent Optical Networks (ICTON)*, Trento, pp. 1–3 (2016).
27. M. K. Eghbal, F. Aminian, and M. Shadaram, "Effect of different optical codes on a W-band WDM-over-OCDMA system," in *19th Int. Conf. Transparent Optical Networks (ICTON)*, Girona, pp. 1–4 (2017).
28. M. K. Eghbal and M. Shadaram, "Tandem dual-electrode Mach Zehnder modulators generating W-band signals for an OCDMA radio-over-fiber system," in *IEEE Photonics Society Summer Topical Meeting Series (SUM)*, San Juan, pp. 213–214 (2017).
29. M. K. Eghbal and M. Shadaram, "W-band radio-over-fiber propagation of two optically encoded wavelength channels," *Opt. Eng.* **57**(1), 016104 (2018).
30. W. Amaya et al., "WDM-Coherent OCDMA over one single device based on short chip super structured fibre Bragg gratings," *Opt. Express* **19**(24), 24627–24637 (2011).
31. X. Wang et al., "High reflectivity superstructured FBG for coherent optical code generation and recognition," *Opt. Express* **12**(22), 5457–5468 (2004).
32. A. H. Aboutalebi and L. Duan, "RAPS: restore-aware policy selection for STT-MRAM-based main memory under read disturbance," in *IEEE 35th Int. Conf. Computer Design (ICCD)*, pp. 625–632 (2017).
33. T. Erdogan, "Fiber grating spectra," *J. Lightwave Technol.* **15**(8), 1277–1294 (1997).
34. H. Kogelnik, "Theory of optical waveguides," in *Guided-Wave Optoelectronics*, T. Tamir, Ed., pp. 74–84, Springer-Verlag, Berlin (1990).
35. J. S. Pereira and H. J. A. da Silva, "Error probability upper bound for perfect sequences implemented with super-structured fibre Bragg gratings," *IET Signal Process.* **8**(4), 421–428 (2014).
36. E. H. Dinan and B. Jabbari, "Spreading codes for direct sequence CDMA and wideband CDMA cellular networks," *IEEE Commun. Mag.* **36**(9), 48–54 (1998).
37. S. Boztas, R. Hammons, and P. Y. Kumar, "4-phase sequences with near-optimum correlation properties," *IEEE Trans. Inf. Theory* **38**(3), 1101–1113 (1992).
38. P. Fan and M. Darnell, *Sequence Design for Communications Applications*, Research Studies Press, Somerset, pp. 225–232 (1996).

Morad Khosravi Eghbal is a postdoctoral fellow in the Electrical and Computer Engineering Department at the University of Texas at San Antonio. He received his PhD in electrical engineering from the University of Texas at San Antonio in 2018. His research interests are millimeter wave RoF networks, free-space optical communications, and WDM optical networks for next-generation mobile communication (5G). He has published more than 12 articles in journals and conference proceedings.

Mehdi Shadaram is the Briscoe distinguished professor and the founding director of the Center for Excellence in Engineering Education at the University of Texas at San Antonio. His main area of research is in the broadband analog and digital fiber optic and wireless systems. He has published more than 120 articles in refereed journals and conference proceedings. He is a senior member of IEEE. He received his PhD in electrical engineering from the University of Oklahoma in 1984.